ARTICLE

3D nanostructured conductive PANI/MXene hydrogels for durable aqueous zinc-ion batteries

Yalei Wang,[a,b] Jun Song,* [b] and Wai-Yeung Wong* [a,c]

Polyaniline (PANI) hydrogels are promising cathode materials for aqueous zinc-ion batteries (AZIBs) due to their inherent porous structure and redox activity. However, the instability during the repeated charge/discharge process limits their application in commercial battery systems. Herein, PANI/MXene hydrogels are synthesized by grafting the negatively charged MXene with the aniline monomer followed by the rapid chemical oxidative polymerization reaction. After combining MXene nanosheets with the PANI chains, the hybrid hydrogels show the three-dimensional (3D) network structure of MXene nanosheets interconnected with PANI chains through hydrogen bond interactions, thus greatly improving the electrochemical reactivity and stability. Moreover, the 3D PANI/MXene network structure can provide fast transport channels for ions and electrons. Consequently, the PANI/MXene cathodes not only achieve high capacity of 219.0 mAh g^{-1} at 0.2 A g^{-1}, but also exhibit outstanding rate performance (147.5 mAh g^{-1} at 5 A g^{-1}), together with excellent long-term cycling stability (over 5000 cycles with a capacity retention of 88.3%). The Zn^{2+} and $CF_3SO_3^-$ insertion/extraction mechanisms are further revealed by ex situ X-ray photoelectron spectroscopy (XPS) measurements. This work demonstrates the availability of conducting polymer hydrogels as cathode materials for high-performance AZIBs.

Introduction

Rechargeable aqueous batteries based on different metal ions including lithium, sodium, potassium, magnesium, aluminum, and zinc have attracted great attention in the field of large-scale energy storage.[1–2] In particular, aqueous zinc-ion batteries (AZIBs) are emerging as promising energy storage devices for practical applications owing to their high theoretical capacity (820 mAh g^{-1}), low redox potential (-0.76 V vs. standard hydrogen electrode), abundant resource, and good compatibility with aqueous electrolytes.[3–7] At present, various cathode materials, such as manganese-based composites,[8–10] vanadium-based composites,[11–13] and organic compounds[14–16] have been studied for Zn^{2+} storage. As compared to the above electrode materials, conducting polymers are found to have high conductivity, facile synthesis procedure, and good environmental stability, resulting in enhanced energy storage capability.[17–18] In recent years, polyaniline (PANI) is probably the most studied conducting polymer in AZIBs, mainly due to its high electrochemical reactivity and low cost.[19] However, PANI cathode materials still have the problems of poor cyclic stability, limited conductivity, and confined active sites, which are caused by aggregated morphology, H^+ deficiency, and irregular structure, respectively.[20–21] Therefore, there is much room for development to improve the electrochemical performance of PANI, especially the long-term cycling stability.

Nevertheless, how to achieve the performance leap of PANI in AZIBs is fraught with challenges. The combination of PANI with two-dimensional (2D) conductive materials is an effective method to improve the overall electrochemical performance. For example, Han et al. prepared the reduced graphene oxide (rGO)@PANI composite hydrogel with three-dimensional (3D) nano-architecture, which exhibits a large capacity of 154 mAh g^{-1} at a current density of 0.1 A g^{-1}, superior rate capability, and excellent cycling performance with a capacity retention of 80.5% after 6000 charge/discharge cycles in the Zn-ion hybrid cell.[22] Compared with rGO, $Ti_3C_2T_x$ (MXene) is a promising 2D material with metallic conductivity, remarkable hydrophilicity, and high mechanical strength, which is produced by selective etching of the Al element layer from the Ti_3AlC_2 phase.[23] Considering the expansion and contraction of PANI backbone chains during the charge/discharge process, the introduction of $Ti_3C_2T_x$ is a good choice to improve the electrochemical performance of PANI materials. Particularly, the hydrogen bonding between oxygen-containing groups on the surface of MXenes and hydrogen atoms in the amine groups of PANI can improve the structural stability and electron conductivity of composites.[24-25] Moreover, it is well recognized that electrochemical reaction is essentially a process at the interface between the electrode and electrolyte solution.[26] Thus, the

large interface area will facilitate rapid electrochemical process. Hydrogels are polymeric networks that have 3D structures with rich porosity, which can provide high specific surface area and promote the transport of ions at the electrolyte/electrode interface.[27] For example, Wang et al. synthesized nanostructured conductive hydrogels using the disc-shaped liquid crystal molecular CuPcTs as the dopant and cross-linking gelator, which increases the contact area between the cathode and electrolyte, promotes the electrolyte permeation into the active particle surface, and hence enhances the reactive kinetics during the charge/discharge process.[28] Inspired by the advantages mentioned above, introducing MXene materials into PANI chains to form the PANI/MXene hydrogel in a simple way is viewed as an attractive electrode structure for AZIBs.

In this work, we report 3D interconnected PANI/MXene hydrogels by the self-assembly of MXene nanosheets and redox-active PANI chains. After the introduction of MXene nanosheets into the PANI chains, the obtained structure not only provides more active sites for PANI, but also increases the conductivity of the PANI chains, thereby facilitating the transport of ions and electrons in PANI/MXene hydrogels. Furthermore, benefiting from the hydrogen bond interaction between MXene nanosheets and PANI chains, the PANI/MXene hydrogel exhibits good structural and electrochemical stability. Specifically, the PANI/MXene cathode delivers a high capacity of 147.5 mAh g^{-1} , and maintains 130.2 mAh g^{-1} at a current density of 5 A g^{-1} after 5000 cycles with a coulomb efficiency of 99.9%. Mechanism study indicates that PANI/MXene cathode not only experiences the redox process between −NH− and −NH^+=, together with the insertion/extraction of the counterions [$CF_3SO_3^-$] from the $Zn(CF_3SO_3)_2$ electrolyte, but also undergoes the redox event between −N= and −N^-–, accompanied by the insertion/extraction of the Zn^{2+}. Our work gives an insight to the design of high-capacity cathode materials, promoting the practical application of AZIBs.

Results and discussion

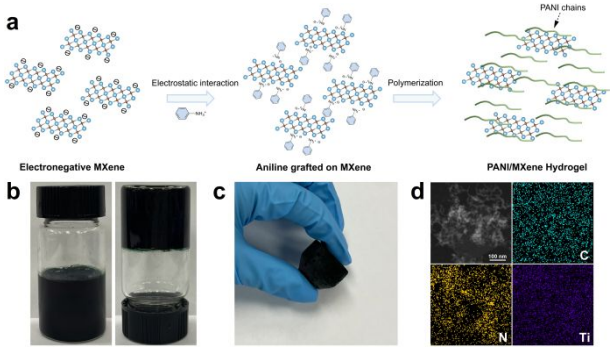

Fig. 1 a) Illustrations for the preparation process of the PANI/MXene hydrogel. b) A photograph of the PANI/MXene hydrogel inside a glass vial. c) A photograph of the PANI/MXene hydrogel after freeze-drying. d) STEM and the corresponding elemental mapping images of the PANI/MXene.

The 3D network gelation process of MXene nanosheets interconnected with PANI chains is illustrated in Fig. 1a. $Ti_3C_2T_x$ MXene nanosheets are obtained by selective etching of the Al layer with tetramethylammonium hydroxide (TMAOH) from the Ti_3AlC_2 MAX phase and subsequent mechanical shaking (Fig. S1-4). Notably, MXene nanosheets are negatively charged due to the presence of some oxygen-containing functional groups on the surface (Fig. S5). Then, the MXene nanosheets are grafted with protonated aniline by the electrostatic interaction. After the introduction of ammonium persulfate, the polymerization of aniline is initiated at 4 °C . Therefore, the PANI/MXene hydrogel is successfully fabricated, which can be proved by a tube inversion method (Fig. 1b), and the dehydrated PANI/MXene is obtained after the freeze-drying (Fig. 1c). The 3D porous network in dehydrated PANI/MXene, consisting of coral-like PANI nanofibers with a uniform diameter of 10-30 nm and MXene nanosheets, is characterized using scanning electron microscopy (SEM) (Fig. S6). Further investigations by scanning transmission electron microscopy (STEM) reveal that the MXene nanosheets are uniformly dispersed in the network and connected to PANI fibers (Fig. 1d). Besides, the elemental mapping images show elements of C, N, and Ti, suggesting that the PANI nanofibers are uniformly combined with MXene nanosheets. Moreover, the N_2 adsorption-desorption isotherms at 77 K of the PANI/MXene (Fig. 2f) show a larger Brunauer–Emmett–Teller (BET) surface area of 244.9 m^2 g^{-1} compared to that of the PANI (181.2 m^2 g^{-1}), thus revealing intrinsically high porosity that can promote the ion transport and electrolyte penetration.[29]

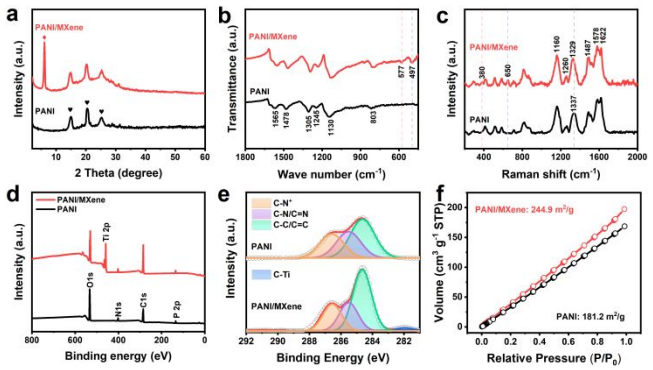

Fig. 2 Structural characterizations for the PANI/MXene and PANI. a) XRD spectra. b) FTIR spectra. c) Raman spectra. d) XPS full spectra. e) XPS C 1s spectra. f) Nitrogen adsorption-desorption isotherms.

The structures of the PANI/MXene and PANI are investigated by the X-ray diffraction (XRD) analysis. As shown in Fig. 2a, three broad peaks at 15.0°, 20.5°, and 25.4° in the PANI can correspond to the (011), (020), and (200) planes of the PANI in the emeraldine salt form, respectively.[27] Compared with the PANI, the PANI/MXene shows a new diffraction peak at the low-angle region, which is attributed to the (002) crystal plane of the $Ti_3C_2T_x$, indicating the successful formation of the PANI/MXene composite structure. Moreover, the characteristic peaks of the PANI in the PANI/MXene show a slight left shift due to the introduction of MXene. The chemical environments of the PANI/MXene and PANI are analyzed by the Fourier transform infrared spectroscopy (FT-IR) (Fig. 2b). For the PANI, the peaks at 1565 and 1478 cm^{-1} are associated with the stretching vibration of quinonoid (Q) and benzenoid (B) rings, indicating that the formed PANI is an emeraldine salt, and the peaks

located at 1305 and 1245 cm^{-1} are ascribed to the C–N stretching vibration in Q–B–Q and B units. while the peaks at 1130 and 803 cm^{-1} are attributed to the C–H bending vibration in the Q and B rings.[30] At the same time, it could be observed that two additional peaks located at 577 and 497 cm^{-1} are detected in the PANI/MXene, corresponding to the Ti–O and Ti–C stretching vibration of the MXene.[31] Notably, the PANI characteristic peaks in the PANI/MXene move to a lower wavenumber compared to the pristine PANI, revealing the existence of the interaction between PANI and MXene, which is possibly derived from the formation of hydrogen bonding. Such peak shifting is also observed in the Raman spectra (Fig. 2c). The signature vibrations of the PANI and MXene can be easily observed in the PANI/MXene. For example, the peaks at 1622, 1578, 1487, 1260, and 1160 cm^{-1} are assigned to the C–C stretching vibration of the B ring, C=C stretching vibration of the Q ring, C=N stretching vibration of the Q ring, C–N stretching vibration of the secondary aromatic amines, and C–H bending vibration of the Q ring, respectively.[32] The peaks at 650 and 380 cm^{-1} are related to the Ti–C and Ti–O stretching vibration of the MXene.[33] Moreover, the peak corresponding to the C–$N^{+\bullet}$ stretching vibration shifts to the lower wavenumber (1329 cm^{-1}) and the intensity increases significantly, revealing more efficient protonation in PANI/MXene.[34] Furthermore, X-ray photoelectron spectroscopy (XPS) is used to study the elemental composition. Fig. 2d exhibits the full survey spectra of the PANI/MXene and PANI. The C 1s spectra of the PANI/MXene can be deconvoluted into four peaks corresponding to C–Ti (282.0 eV), C–C/C=C (284.6 eV), C–N/C=N (285.5 eV), and C–N^{+} (286.6 eV), respectively (Fig. 2e). Noticeably, the signal of C–Ti is generated after the introduction of MXene, resulting in high conductivity, which is beneficial to improve the electrochemical performance.[35]

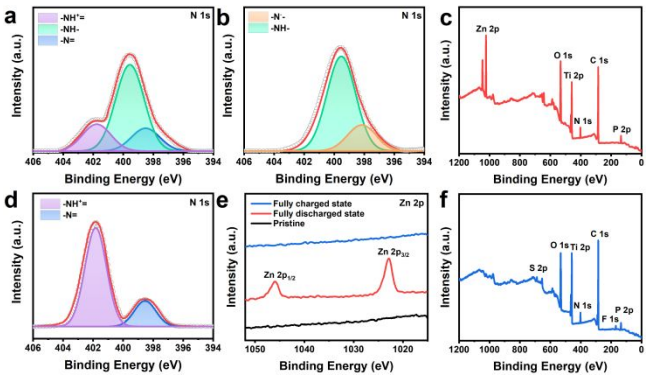

Fig. 3 a, b, d) High-resolution XPS N 1s spectra of the PANI/MXene electrode in pristine, fully discharged, and fully charged states. e) High-resolution XPS Zn 2p spectra of the PANI/MXene electrode. c, f) XPS full spectra of the PANI/MXene electrode in fully discharged and fully charged states.

Ex situ XPS is applied to elucidate the variation of N and Zn components in the PANI/MXene during the charge/discharge process. As shown in Fig. 3a, the pristine N 1s can be split into three peaks located at 401.8, 399.6, and 398.5 eV, which are ascribed to –NH^{+}=, –NH–, and –N=, respectively.[36] It should be noted that the –NH^{+}= and –N= correspond to the oxidized state, while the –NH– belongs to the reduced state. When the PANI/MXene electrode is fully discharged to 0.5 V, –NH^{+}= and –N= are completely reduced, accompanied by the increase of –NH– and appearance of –N^{-}– (Fig. 3b). Meanwhile, the Zn signal is detected in the full spectra and high-resolution Zn 2p spectra (Fig. 3c, e), indicating the Zn^{2+} intercalation during the discharge process. At the following fully charged state (1.5 V), the peaks of –NH^{+}= and –N= appear, along with the oxidation of –NH– and –N^{-}– (Fig. 3d). Besides, the peak of Zn 2p disappears (Fig. 3e), and the peaks of S 2p (169.1 eV) and F 1s (688.1 eV) are observed in the fully charged state (Fig. 3f). These results indicate that Zn^{2+} interacts with reduced PANI/MXene at the discharged state, while $CF_3SO_3^-$ interacts with oxidized PANI/MXene at the charged state. That is to say, PANI/MXene cathode shows the dual-ion mechanism that combines the Zn^{2+} and $CF_3SO_3^-$ insertion/extraction.

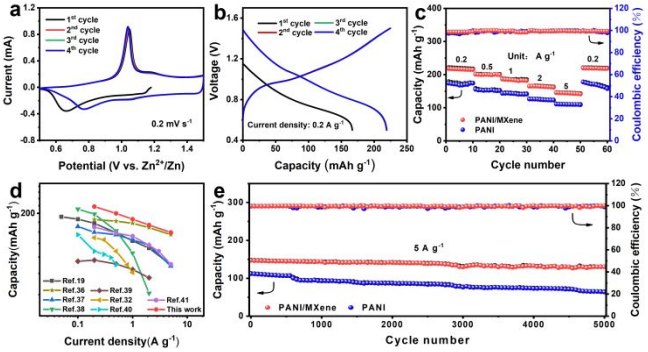

Fig. 4 The electrochemical performance of the PANI/MXene cathode. a) CV curves at 0.2 mV s^{-1}. b) Galvanostatic charge/discharge curves at 0.2 A g^{-1}. c) Rate performance of the PANI/MXene and PANI. d) Comparison of the rate performance among our PANI/MXene and reported PANI cathodes for AZIBs. e) Cycling performance of the PANI/MXene and PANI at 5 A g^{-1}.

The electrochemical performance of the PANI/MXene cathode is investigated in the coin-cell type AZIBs by using 2 M zinc trifluoromethanesulfonate ($Zn(CF_3SO_3)_2$) aqueous solution as the electrolyte. The cyclic voltammetry (CV) curves in Fig. 4a exhibit two pairs of redox peaks at about 0.77/1.05 and 1.06/1.18 V, corresponding to the intercalation/extraction of Zn^{2+} and the interaction between $CF_3SO_3^-$ and –NH^{+}= in PANI/MXene.[37] More importantly, the subsequent CV curves are almost overlapped after the first cycle, suggesting the highly reversible redox reaction. The PANI/MXene cathode displays high reversible discharge capacity of 219.0 mAh g^{-1} at 0.2 A g^{-1} (Fig. 4b). Moreover, the rate performance of the PANI/MXene and PANI is shown in Fig. 4c. More specifically, the average discharge capacities of the PANI/MXene are 219.3, 200.1, 184.9, 165.9, and 144.6 mA h g^{-1} at increasing current density from 0.2, 0.5, 1, 2, to 5 A g^{-1}, respectively (Fig. S8), displaying competitive electrochemical performance in comparison with other previously reported PANI-based cathode materials (Fig. 4d). When the current density returns from 5 to 0.2 A g^{-1} after 50 cycles, the corresponding discharge capacity can still be restored to 217.6 mAh g^{-1}, which shows significantly enhanced rate performance compared to the PANI (Fig. S9). In addition, the long-term cycling performance was carried out at 5 A g^{-1} (Fig. 4e). The PANI/MXene cathode can still deliver high discharge capacity of 130.2 mAh g^{-1} after 5000 cycles, achieving an impressive capacity retention of 88.3%. In contrast, the PANI cathode exhibits faster capacity decay, with a capacity retention

of 56.9% after 5000 cycles. It is worth noting that the crystal structure and morphology of the PANI/MXene cathode have not changed significantly even after 5000 cycles (Fig. S10, 11). Consequently, the high structural stability of the PANI/MXene cathode during repeated charge/discharge process ensures excellent long-term cycling performance.

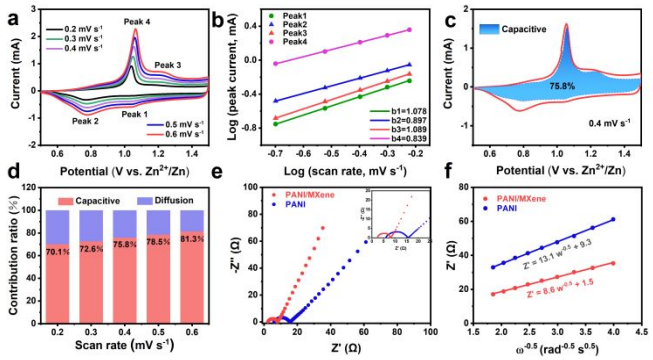

Fig. 5 The electrochemical kinetics of the PANI/MXene cathode. a) CV curves at various scan rates. b) log ν vs. log i plots according to the CV curves. c) The CV curve with a capacitive contribution at 0.4 mV s^{-1}. d) The capacitive contribution ratios at various scan rates. e) Nyquist plots of the PANI/MXene and PANI. f) The relationship between the low frequency and real part of the impedance.

The excellent rate performance of the PANI/MXene cathode is largely dependent on its reaction kinetics, which is studied in detail by the CV curves at various scan rates (Fig. 5a). The peak current (i) and scan rate (v) follow the equation:[42] $i = a\,v^b$, where a and b represent adjustable parameters. It can be rearranged as follows: $\log i = \log a + b \log v$. If the value of b is 0.5, it indicates the diffusion-controlled process, while if the value of b is 1.0, that suggests the capacitive-controlled process. As displayed in Fig. 5b, the b values of peaks 1, 2, 3, and 4 are 1.078, 0.897, 1.089, and 0.839, respectively, these manifest that the energy storage process in PANI/MXene is mainly dominated by the capacitive behavior. Furthermore, the capacitive contribution ratio at different scan rates can be obtained according to the equation:[43] $i = k_1 v + k_2 v^{1/2}$, where $k_1 v$ and $k_2 v^{1/2}$ correspond to the capacitive-controlled contribution and diffusion-controlled contribution. The capacitive contribution ratio rises from 70.1% to 81.3% as the scan rate gradually increases from 0.2 to 0.6 mV s^{-1} (Fig. 5c, d). In addition, the galvanostatic intermittent titration technique (GITT) is utilized to determine the ion diffusion coefficient (D_{ion}) in the PANI/MXene cathode (details shown in the Supporting Information).[44] The D_{ion} values are in the range of 1.30×10^{-9} and 2.58×10^{-8} cm^2 s^{-1} (Fig. S12), which is higher than the most previously reported PANI-based cathode materials. Moreover, such fast kinetics can also be reflected by the electrochemical impedance spectroscopy (EIS) measurement.[45] Noticeably, the PANI/MXene cathode shows smaller charge transfer impedance (R_{ct}) of 5.5 Ω compared to the PANI cathode (9.7 Ω) (Fig. 5e), clearly indicating faster charge transfer process at the electrode/electrolyte interface in our PANI/MXene system. Furthermore, the relationship between the low frequency (ω) and real impedance (Z') of EIS can be used to calculate the ion diffusion coefficients (details shown in the Supporting Information).[46] The D_{ion} of the PANI/MXene is calculated to be 1.53×10^{-9} cm^2 s^{-1} (Fig. 5f), which is in good agreement with the GITT results. The fast kinetics endow PANI/MXene cathodes with excellent rate performance.

Experimental Section

Preparation of the $Ti_3C_2T_x$ MXene nanosheets

In a typical synthesis process, 1.0 g of Ti_3AlC_2 powder was treated with 10 wt.% hydrofluoric acid (HF) in an ambient environment. After stirring for 15 min, the resulting suspension was centrifuged and washed with deionized (DI) water several times until the pH reached 7. Then, HF-pretreated sample was immersed in aqueous tetramethylammonium hydroxide (TMAOH) (12.5 wt%, 10 mL) and reacted for 24 h under stirring to etch the interlayer Al layers. The bottom slurry was washed several times by centrifuging with DI water until the supernatant solution became neutral and then collected. By redispersing the slurry in DI water and shaking for 12 h, the final $Ti_3C_2T_x$ MXene nanosheets were obtained for further characterization and use.

Preparation of the PANI/MXene hydrogels

PANI/MXene hydrogel electrodes were made via the following solution process. First, 0.286 g (1.25 mmol) ammonium persulfate was dissolved in 1 mL DI water (solution A). Second, 0.5 mL $Ti_3C_2T_x$ MXene nanosheets (1 mg mL^{-1}) were dispersed in a monomer solution containing 0.3 mL aniline and 1 mL phytic acid (50%, wt/wt in water) (solution B). To initiate the polymerization, the A and B solutions were cooled to 4 °C and then mixed quickly. In about 5 min, the mixed solution changed colour from brown to dark green, indicating the completion of the in-situ polymerization. The PANI/MXene hydrogel was purified by washing with DI water several times to remove excess acid and byproducts. Finally, the dehydrated PANI/MXene was obtained after freeze-drying. The PANI hydrogel as the control sample was made via the same process by mixing the two solutions (solution A and solution B) without adding $Ti_3C_2T_x$ solution (Fig. S7).

Characterizations

The morphology of the samples was observed using the scanning electron microscope (SEM, FEI Helios Nanolab 600i) and transmission electron microscope (TEM, FEI Tecnai G2 F30) with the energy dispersive spectroscopy (EDS) for the elemental analysis. The structure of the samples was characterized by the D-MAX 2200 VPC X-ray diffractometer (XRD). Fourier transform infrared (FTIR) spectra were recorded using the NEXUS 870 spectrophotometer. Raman spectra were measured on the Renishaw inVia-Reflex03040405 spectrometer. X-ray photoelectron spectroscopy (XPS) was collected through the Thermo Scientific ESCLAB 250Xi spectrometer. The specific surface area was obtained at 77 K with the Quadrasorb SI-MP system.

Electrochemical Measurements

The electrochemical performance was measured by using the cyclic voltammetry (CV), galvanostatic charge/discharge (GCD), electrochemical impedance spectra (EIS), and galvanostatic intermittent titration technique (GITT) in a coin-type cell with the PANI/MXene hydrogel as the working electrode and the zinc foil as the counter/reference electrode. 2 M zinc trifluoromethanesulfonate ($Zn(CF_3SO_3)_2$) aqueous solution and glass fiber were used as the electrolyte and separator. The dehydrated PANI/MXene was cut into 12 mm discs and compressed onto the steel mesh for use as the working electrode. The mass loading of active materials was about 1.5 mg cm^{-2}. All cells were aged for 2 h before starting the electrochemical test to ensure adequate penetration of the electrolyte into the electrodes.

Calculations of the Ion Diffusion Coefficients (D_{ion})

The main text of the article should appear here with headings as appropriate. The ion diffusion coefficient (D_{ion}) in the PANI/MXene cathode was tested by the EIS and calculated based on the equation as follows:[47, 48]

$$Z' = R_s + R_f + R_{ct} + \sigma_w \omega^{-0.5}$$

$$D_{ion} = \frac{R^2T^2}{2A^2n^4F^4C^2\sigma_w^2}$$

where *R, T and F* represent the gas constant (8.314 J $mol^{-1}\cdot K^{-1}$), absolute temperature (298 K), and Faraday constant (96500 C mol^{-1}), respectively; *A, n and C* correspond to the electrode surface area, number of transferred electrons, and concentration of ions, respectively; σ_w is the linear fitting slope from the relationship between the low frequency and real part of impedance.

In additon, the ion diffusion coefficient (D_{ion}) can also be calculated by the GITT measurements based on the following equation:[49]

$$D_{ion} = \frac{4L^2}{\pi\tau}\left(\frac{\Delta E_s}{\Delta E_\tau}\right)^2$$

where τ, *L and* ΔE_τ stand for the constant current pulse time, ion diffusion length, and voltage change induced by the galvanostatic charge/discharge process, respectively; ΔE_s is the voltage change between two adjacent equilibrium states. The galvanostatic intermittent titration technique (GITT) was carried out with the pulse of 0.2 A g^{-1} for 4 min and 180 min interruption after each pulse to make the voltage reach equilibrium.

Conclusions

In summary, we have developed the 3D network of MXene nanosheets interconnected with PANI chains through the electrostatic interaction between negatively charged MXene nanosheets and protonated aniline monomers. The 3D network structure makes it easier for electrolyte ions to contact the electrode material, thereby promoting the ion transport. After introducing the MXene nanosheets into the PANI chains, the PANI/MXene cathode provides fast transport channel for the electron transfer in the redox reactions of electrode materials. More importantly, the interactions between MXene nanosheets and PANI chains give the composite cathode good structural stability. Therefore, the PANI/MXene cathode manifests superior electrochemical performance in terms of high reversible capacity (219.0 mAh g^{-1} at a current density of 0.2 A g^{-1}), superior rate performance (147.5 mAh g^{-1} at a current density of 5 A g^{-1}), and good cyclic stability (capacity retention of 88.3% even after 5000 cycles). In addition, ex situ XPS studies reveal the dual-ion mechanism that combines the Zn^{2+} and $CF_3SO_3^-$ insertion/extraction. These results illustrate the PANI/MXene hydrogels will have a broad prospect as cathode materials for AZIBs in the future.

Conflicts of interest

There are no conflicts to declare.

Acknowledgements

This work was supported by the National Natural Science Foundation of China (52102268/62175161/61835009/ 62127819/61905120/52073242), the RGC Senior Research Fellowship Scheme (SRFS2021-5S01), National Key R&D Program of China (2021YFF0502900), Shenzhen Science and Technology Program (JCYJ20210324095810028), Shenzhen Key Laboratory of Photonics and Biophotonics (ZDSYS20210623092006020), the Hong Kong Research Grants Council (PolyU 15307321), Miss Clarea Au for the Endowed Professorship in Energy (847S), and Research Institute for Smart Energy (CDAQ) for financial support.

Notes and references

1 Y. Liang and Y. Yao, *Nat. Rev. Mater.*, 2022, **8**, 109-122.
2 H. Wang, R. Tan, Z. Yang, Y. Feng, X. Duan and J. Ma, *Adv. Energy Mater.*, 2020, **11**, 2000962.
3 L. Cao, D. Li, T. Pollard, T. Deng, B. Zhang, C. Yang, L. Chen, J. Vatamanu, E. Hu, M. J. Hourwitz, L. Ma, M. Ding, Q. Li, S. Hou, K. Gaskell, J. T. Fourkas, X. Q. Yang, K. Xu, O. Borodin and C. Wang, *Nat. Nanotechnol.*, 2021, **16**, 902-910.
4 A. Clarisza, H. K. Bezabh, S. K. Jiang, C. J. Huang, B. W. Olbasa, S. H. Wu, W. N. Su and B. J. Hwang, *ACS Appl. Mater. Interfaces*, 2022, **14**, 36644-36655.
5 S. Liu, L. Kang, J. M. Kim, Y. T. Chun, J. Zhang and S. C. Jun, *Adv. Energy Mater.*, 2020, **10**, 2000477.
6 A. Konarov, N. Voronina, J. H. Jo, Z. Bakenov, Y.-K. Sun and S.-T. Myung, *ACS Energy Lett.*, 2018, **3**, 2620-2640.
7 G. Fang, J. Zhou, A. Pan and S. Liang, *ACS Energy Lett.*, 2018, **3**, 2480-2501.
8 8. J. Wang, J. G. Wang, H. Liu, Z. You, Z. Li, F. Kang and B. Wei, *Adv. Funct. Mater.*, 2020, **31**, 2007397.
9 9. X. Zhu, Z. Cao, W. Wang, H. Li, J. Dong, S. Gao, D. Xu, L. Li, J. Shen and M. Ye, *ACS Nano*, 2021, **15**, 2971-2983.

10 X. Gao, H. Wu, W. Li, Y. Tian, Y. Zhang, H. Wu, L. Yang, G. Zou, H. Hou and X. Ji, *Small*, 2020, **16**, 1905842.
11 S. Deng, Z. Yuan, Z. Tie, C. Wang, L. Song and Z. Niu, *Angew. Chem. Int. Ed.*, 2020, **59**, 22002-22006.
12 X. Wang, Y. Li, S. Wang, F. Zhou, P. Das, C. Sun, S. Zheng and Z. S. Wu, *Adv. Energy Mater.*, 2020, **10**, 2000081.
13 H. Liu, L. Jiang, B. Cao, H. Du, H. Lu, Y. Ma, H. Wang, H. Guo, Q. Huang, B. Xu and S. Guo, *ACS Nano*, 2022, **16**, 14539-14548.
14 N. Zhang, X. Chen, M. Yu, Z. Niu, F. Cheng and J. Chen, *Chem Soc Rev*, 2020, **49**, 4203-4219.
15 Z. Tie, L. Liu, S. Deng, D. Zhao and Z. Niu, *Angew. Chem. Int. Ed.*, 2020, **59**, 4920-4924.
16 L. Yan, Y. Zhang, Z. Ni, Y. Zhang, J. Xu, T. Kong, J. Huang, W. Li, J. Ma and Y. Wang, *J. Am. Chem. Soc.*, 2021, **143**, 15369-15377.
17 C. Kim, B. Y. Ahn, T. S. Wei, Y. Jo, S. Jeong, Y. Choi, I. D. Kim and J. A. Lewis, *ACS Nano*, 2018, **12**, 11838-11846.
18 M. Y. Zhang, Y. Song, X. Mu, D. Yang, Z. Qin, D. Guo, X. Sun and X. X. Liu, *Small*, 2022, **18**, 2107689.
19 F. Wan, L. Zhang, X. Wang, S. Bi, Z. Niu and J. Chen, *Adv. Funct. Mater.*, 2018, **28**, 1804975.
20 J. Huang, Z. Wang, M. Hou, X. Dong, Y. Liu, Y. Wang and Y. Xia, *Nat. Commun.*, 2018, **9**, 2906.
21 J. Zeng, Z. Zhang, X. Guo and G. Li, *J. Mater. Chem. A*, 2019, **7**, 21079-21084.
22 J. Han, K. Wang, W. Liu, C. Li, X. Sun, X. Zhang, Y. An, S. Yi and Y. Ma, *Nanoscale*, 2018, **10**, 13083-13091.
23 S. Nam, M. Mahato, K. Matthews, R. W. Lord, Y. Lee, P. Thangasamy, C. W. Ahn, Y. Gogotsi and I. K. Oh, *Adv. Funct. Mater.*, 2022, **33**, 2210702.
24 Z. Chen, Y. Wang, J. Han, T. Wang, Y. Leng, Y. Wang, T. Li and Y. Han, *ACS Appl. Energy Mater.*, 2020, **3**, 9326-9336.
25 M. Boota, B. Anasori, C. Voigt, M. Q. Zhao, M. W. Barsoum and Y. Gogotsi, *Adv. Mater.*, 2016, **28**, 1517-1522.
26 X. He, D. Bresser, S. Passerini, F. Baakes, U. Krewer, J. Lopez, C. T. Mallia, Y. Shao-Horn, I. Cekic-Laskovic, S. Wiemers-Meyer, F. A. Soto, V. Ponce, J. M. Seminario, P. B. Balbuena, H. Jia, W. Xu, Y. Xu, C. Wang, B. Horstmann, R. Amine, C.-C. Su, J. Shi, K. Amine, M. Winter, A. Latz and R. Kostecki, *Nat. Rev. Mater.*, 2021, **6**, 1036-1052.
27 P. Li, Z. Jin, L. Peng, F. Zhao, D. Xiao, Y. Jin and G. Yu, *Adv. Mater.*, 2018, **30**, 1800124.
28 Y. Wang, Y. Shi, L. Pan, Y. Ding, Y. Zhao, Y. Li, Y. Shi and G. Yu, *Nano Lett.*, 2015, **15**, 7736-7741.
29 X. Shen, X. Wang, Y. Zhou, Y. Shi, L. Zhao, H. Jin, J. Di and Q. Li, *Adv. Funct. Mater.*, 2021, **31**, 2101579.
30 L. Yang, S. Wang, J. Mao, J. Deng, Q. Gao, Y. Tang and O. G. Schmidt, *Adv. Mater.*, 2013, **25**, 1180-1184.
31 Z. Wang, J. Xuan, Z. Zhao, Q. Li and F. Geng, *ACS Nano*, 2017, **11**, 11559-11565.
32 X. Xiao, W. Liu, K. Wang, C. Li, X. Sun, X. Zhang, W. Liu and Y. Ma, *Nanoscale Adv*., 2020, **2**, 296-303.
33 W. Liu, Z. Wang, Y. Su, Q. Li, Z. Zhao and F. Geng, *Adv. Energy Mater.*, 2017, **7**, 1602834.
34 Y. Liu, L. Xie, W. Zhang, Z. Dai, W. Wei, S. Luo, X. Chen, W. Chen, F. Rao, L. Wang and Y. Huang, *ACS Appl Mater Interfaces*, 2019, **11**, 30943-30952.
35 J. Wu, Q. e. Zhang, J. Wang, X. Huang and H. Bai, *Energy Environ. Sci.*, 2018, **11**, 1280-1286.
36 H. Y. Shi, Y. J. Ye, K. Liu, Y. Song and X. Sun, *Angew. Chem. Int. Ed.*, 2018, **57**, 16359-16363.
37 M. Yao, Z. Yuan, S. Li, T. He, R. Wang, M. Yuan and Z. Niu, *Adv. Mater.*, 2021, **33**, 2008140.
38 H. Cao, F. Wan, L. Zhang, X. Dai, S. Huang, L. Liu and Z. Niu, *J. Mater. Chem. A*, 2019, **7**, 11734-11741.
39 H. Yu, G. Liu, M. Wang, R. Ren, G. Shim, J. Y. Kim, M. X. Tran, D. Byun and J. K. Lee, *ACS Appl Mater Interfaces*, 2020, **12**, 5820-5830.
40 Q. Liu, Z. Ma, Z. Chen, M. Cui, H. Lei, J. Wang, J. Fei, N. He, Y. Liu, Q. Liu, W. Li and Y. Huang, *Chem. Commun.*, 2022, **58**, 8226-8229.
41 G. Shim, M. X. Tran, G. Liu, D. Byun and J. K. Lee, *Energy Storage Mater.*, 2021, **35**, 739-749.
42 S. Deng, Z. Tie, F. Yue, H. Cao, M. Yao and Z. Niu, *Angew. Chem. Int. Ed.*, 2022, **61**, e202115877.
43 S. Chen, K. Li, K. S. Hui and J. Zhang, *Adv. Funct. Mater.*, 2020, **30**, 2003890.
44 Y. Yang, Y. Tang, G. Fang, L. Shan, J. Guo, W. Zhang, C. Wang, L. Wang, J. Zhou and S. Liang, *Energy Environ. Sci.*, 2018, **11**, 3157-3162.
45 S. Liu, H. Zhu, B. Zhang, G. Li, H. Zhu, Y. Ren, H. Geng, Y. Yang, Q. Liu and C. C. Li, *Adv. Mater.*, 2020, **32**, 2001113.
46 Z. Tie, S. Deng, H. Cao, M. Yao, Z. Niu and J. Chen, *Angew. Chem. Int. Ed.*, 2022, **61**, e202115180.
47 C. Liu, Z. Neale, J. Zheng, X. Jia, J. Huang, M. Yan, M. Tian, M. Wang, J. Yang, G. Cao, *Energy Environ. Sci.* 2019, **12**, 2273-2285.
48 S. Wang, S. Huang, M. Yao, Y. Zhang, Z. Niu, *Angew. Chem. Int. Ed.* 2020, **59**, 11800-11807.
49 M. Liao, J. Wang, L. Ye, H. Sun, Y. Wen, C. Wang, X. Sun, B. Wang, H. Peng, *Angew. Chem. Int. Ed.* 2020, **59**, 2273-2278.